AGU PUBLICATIONS

Geophysical Research Letters

RESEARCH LETTER
10.1002/2015GL065789

**Key Points:**
- The first in situ lunar phase curve since the Apollo era covers phase angle range of 2–141°
- Both shadow hiding and coherent backscattering contribute to the opposition surge
- Single-particle scattering has backward and forward scattering lobes and regolith porosity is obtained

**Supporting Information:**
- Supporting Information S1

**Correspondence to:**
H. Zhang,
um_zhanghao@yahoo.com

**Citation:**
Jin, W., et al. (2015), In situ optical measurements of Chang'E-3 landing site in Mare Imbrium: 2. Photometric properties of the regolith, *Geophys. Res. Lett.*, *42*, 8312–8319, doi:10.1002/2015GL065789.

Received 26 AUG 2015
Accepted 19 SEP 2015
Accepted article online 25 SEP 2015
Published online 21 OCT 2015



# In situ optical measurements of Chang'E-3 landing site in Mare Imbrium: 2. Photometric properties of the regolith

**Weidong Jin[1], Hao Zhang[1], Ye Yuan[1], Yazhou Yang[1], Yuriy G. Shkuratov[2], Paul G. Lucey[3], Vadim G. Kaydash[2], Meng-Hua Zhu[4], Bin Xue[5], Kaichang Di[6], Bin Xu[6], Wenhui Wan[6], Long Xiao[1], and Ziwei Wang[1]**

[1]Planetary Science Institute, School of Earth Sciences, China University of Geosciences, Wuhan, China, [2]Astronomical Institute, Kharkov V.N. Karazin National University, Kharkov, Ukraine, [3]Hawaii Institute of Geophysics and Planetology, University of Hawaii, Honolulu, Hawaii, USA, [4]Space Science Institute, Macau University of Science and Technology, Taipa, Macau, [5]Xi'an Institute of Optics and Precision Mechanics, Chinese Academy of Sciences, Xi'an, China, [6]State Key Laboratory of Remote Sensing Science, Institute of Remote Sensing and Digital Earth, Chinese Academy of Sciences, Beijing, China

**Abstract** The panorama cameras onboard the Yutu Rover of the Chang'E-3 lunar mission acquired hundreds of high-resolution color images of the lunar surface and captured the first in situ lunar opposition effect (OE) since the Apollo era. We extracted the phase curve and the color ratio in three bands with the phase angle range from 2° to 141°. Photometric inversions using the Hapke model reveal that submicroscopic dusts are present in the landing area and both the coherent backscattering and the shadow hiding are responsible for the strong OE. Compared with spaceborne measurements, the grains in the landing site are brighter, more transparent, and appear to be better crystallized than the average maria basaltic grains. The results show that the phase-reddening effect appears to be present in the in situ phase curves. The current phase curve can be used as the ground-truth validations of any future spaceborne phase curve measurement over the landing site region.

## 1. Introduction

Optical measurements of the Moon can be categorized into three broad types: spectroscopic, polarimetric, and photometric measurements [e.g., *Ohtake et al.*, 2013; *Dollfus and Bowell*, 1971; *Shkuratov et al.*, 2011, 2015]. Compared with the spectroscopic features which reveal mineral and chemical compositions, the phase curve, and especially the opposition effect (OE), is more sensitive to regolith's physical properties including particle size distributions, grain transparency, porosity, and packing structures [e.g., *Hapke*, 2012; *Hapke et al.*, 2012; *Shkuratov et al.*, 2011]. The most prominent feature of the lunar OE is a nonlinear surge toward the opposition at small phase angles, and it may be caused by the shadow hiding opposition effect (SHOE) and/or the coherent backscattering opposition effect (CBOE). Photometric models have been developed to quantitatively retrieve regolith's physical properties from measured phase curves [e.g., *Hapke*, 2012; *Shkuratov et al.*, 2011]. During the last two decades, many spaceborne measurements of the lunar phase curve such as the Clementine [*Buratti et al.*, 1996], the Moon Mineralogy Mapper [*Kaydash et al.*, 2013a], the Kaguya [*Yokota et al.*, 2011], and the Lunar Reconnaissance Orbiter (LRO) [*Sato et al.*, 2014] missions have become available. In contrast, in situ quantitative digital measurement of the lunar phase curve had never been carried out until the successful landing of the Chang'E-3 (CE3) mission in northern Mare Imbrium near 340.49°E and 44.12°N in December 2013 [*Xiao et al.*, 2015]. The Yutu Rover roved more than 100 m (with a final resting place 22 m away from the lander) from 15 December 2013 to 14 January 2014, and its onboard panorama cameras performed the first quantitative measurement of the lunar phase curve using its panoramic capability, including the first in situ OE measurement since the Apollo era.

In this letter, we first describe the panoramic camera (PCAM) measurement of the phase curve and the calibration procedures in section 2. Then in section 3 photometric inversions using the Hapke model are presented. We also compare the fitting parameters of the in situ measurement with that derived from remote measurement by the LRO instrument [*Sato et al.*, 2014] in section 4. Possible phase-reddening effects are discussed in section 5. Conclusion and summary are given in section 6.

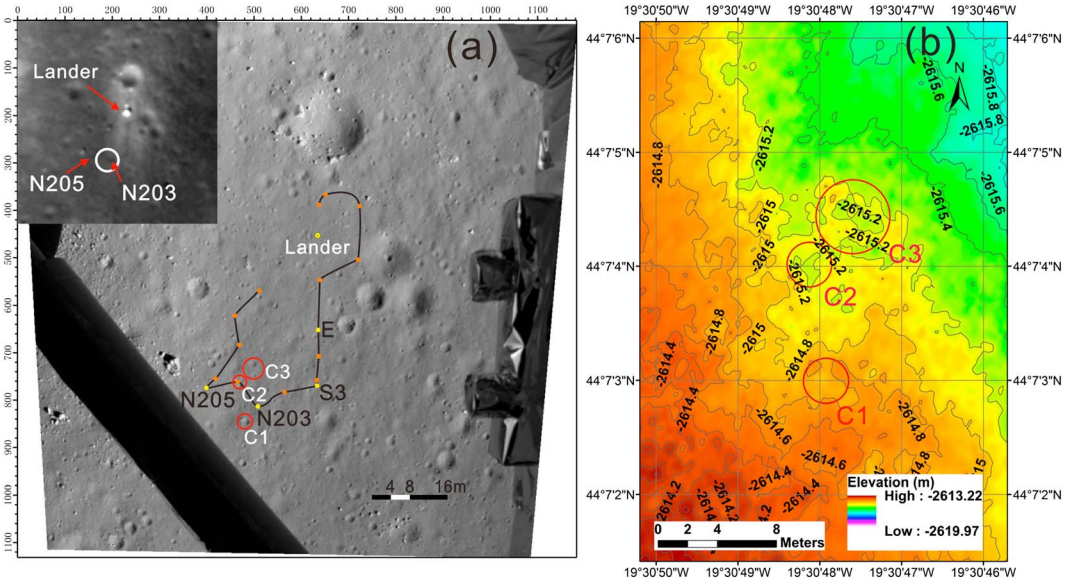


**Figure 1.** The study area of the phase curve. (a) Orthorectified image of the landing area taken by the Landing Camera. The lander position and the rover's path are indicated. The inset is a Lunar Reconnaissance Orbiter Camera image taken on 17 February 2014 showing the increased surface albedo after landing. E, S3, N203, and N205 mark the VNIS measurement locations. (b) DEM of the study region. C1, C2, and C3 are the three tiny craters also indicated in Figure 2.

## 2. Instrument, Measurement, and Phase Curve Extractions

Figure S1 in the supporting information is an image of the Yutu Rover taken by the CE3 lander shortly after rover deployment. On top of the mast are two panoramic cameras (PCAMs) and two navigation cameras (NCAMs) with alternating arrangement as indicated by the white arrows (the arrangement is PCAM 1 (P1), NCAM 1 (N1), PCAM 2 (P2), and NCAM 2 (N2)). Both PCAMs can rotate in horizontal (0–360°) and vertical (−30–0°) directions and the pointing directions in horizontal of the two always turn to each other by 1° so part of their scenes overlaps. The specifications of the PCAMs are summarized in Table S1 in the supporting information.

Figure 1a displays the landing site vicinity observed by the landing camera on board the CE3 lander during the final descent stage. Node E, Node S3, Node N203, and Node N205 are locations where four visible-near-infrared spectroscopic (VNIS) measurements were carried out. Figure 1b is the digital elevation model (DEM) of the landing area, and it shows that this region is macroscopically flat with the maximum and minimum height of −2613.22 and −2619.97 m respectively, with respect to the average radius of the Moon, which is 1737.4 km. Figure 2 displays the strong OE centered around the shadow of the rover mast captured by the P1. This image is a mosaic of 16 overlapping level 2C images (see below) that form a circular area with ~20 m diameter as indicated by the white circle in the inset of Figure 1a. The three tiny craters, C1, C2, and C3, as indicated in Figures 1 and 2, are used to locate the study area where the in situ phase curve was

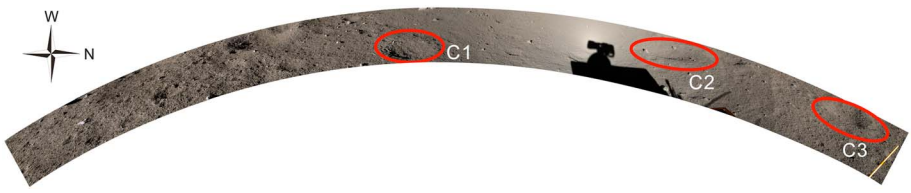


**Figure 2.** The study area of the phase curve imaged by the PCAM (P1). This image is a mosaic of 16 overlapping images that form a circular area with ~20 m diameter as indicated by the white circle in the inset of Figure 1a. The lunar opposition effect is seen centered around the shadow of the P1 camera. The three small craters circled by red ovals are used to identify the study areas shown in Figures 1a and 1b. When these images were taken, the distance of the rover to the lander was 44 m and the rover coordinate was (340.490561°E, 44.118516°N). The average solar incident angle was 70°.

extracted. Obviously, the lunar surface that shows the strong opposition surge is located in the region between Node N203 and N205 and is relatively far from the landing engine blown site. Even so, the blowing may still significantly influence the phase function of the lunar surface, as indicated by earlier studies [*Kaydash et al.*, 2013b; *Shkuratov et al.*, 2013].

The PCAM data products provided by the payload team consist of the sequence of level 0 (L0) to level 2 (L2) images. A detailed description of the data products can be found in *Tan et al.* [2014], and the following is a brief summary. The L0 data correspond to the raw signals measured, whereas the L1 data are the frame transformed from the original L0 data by format processing, and the unit becomes digital number (DN). L2A data are then obtained after performing dark current subtraction and flat fielding corrections using calibration matrices measured in preflight experiments. In addition, information including gain and exposure time is added. The L2B data in DN are obtained by adding geometric information to the corresponding L2A data. The geometric information includes the solar zenith angle, solar azimuth angle, the exterior orientation elements T1, and the inner orientation elements T2. Finally, the L2C data are obtained after performing color calibrations.

To extract the phase curve from the images and perform quantitative photometric analysis, the reflectance value, the phase angle, and the viewing zenith (or emergence angle) of each pixel should be obtained. We first notice that the vector from the pixel to the camera can be calculated with given T1 and T2 by using the collinearity equation and thus the emergence angle is obtained. Next, the vector from the pixel to the Sun can be easily calculated with known values of solar zenith angle and solar azimuth angle. Then the phase angle $\alpha$, which is the angle between these two vectors, of every pixel can be obtained using simple vector algebra. We plot the phase angle as contour map and lay it on top of Figure 2 (notice that the original image of Figure S2 in the supporting information is a single frame of the 16 images that formed Figure 2). Although the minimum phase angle in Figure 2 is about 1.5°, the fuzzy nature of the rover shadow edges may complicate the brightness retrieval near 0° and thus the region within the red lines in Figure S2 is excluded in phase curve extractions. For this reason the minimum phase angle in the retrieved phase curve is truncated to 2°. To retrieve the phase curve over larger phase angle ranges, we used 12 L2B images captured by the P1. To reduce albedo variations at the same phase angles caused by surface heterogeneities and inhomogeneities, we averaged the DN values of pixels within 1° phase angle. The accurate extraction of the phase curve would require two additional conditions. The first one is that the PCAMs have accurate attitude parameters. The second one is that the measured terrain is flat and homogeneous. The first condition is satisfied as when the contour plot of the phase angles computed by this approach is laid on top of the original imagery, it is found that the constant phase angle levels form concentric rings centered around the opposition (the center of P1's shadow), as shown in Figure S2. Thus, the algorithms used to compute the emergence angles should be valid. The second condition is also satisfied as we have shown earlier in Figure 1b that the region under study is rather flat. After averaging pixels having the same phase angle, the residual topography effect will be smoothed out. In addition, pixels containing resolvable fragments and tiny craters are excluded in phase curve extractions to ensure the homogeneity of the observed region.

Each L2B frame contains 2352 by 1728 pixels and consists of four color bands (with the approximate center wavelengths indicated in parenthesis) with Bayer filter (https://en.wikipedia.org/wiki/Bayer_filter) mosaic arrangement: red (640 nm), green (540 nm), green (540 nm), and blue (470 nm) [*Ren et al.*, 2014]. To compensate for the different gains and exposure times of different frames in the mosaic, each L2B frame is divided by a working mode normalization parameter $A_{\mathrm{Cali}}$ recorded in header files to normalize the brightness; then we use the absolute radiation calibration coefficients $C_{\mathrm{Rad}}$ obtained in preflight calibrations to convert the L2B DN values to radiance as

$$I_s = \frac{\mathrm{DN}}{A_{\mathrm{Cali}} \bullet C_{\mathrm{Rad}}}, \tag{1}$$

where $C_{\mathrm{Rad}}$ (in Sr nm cm$^2$/W) is $5.9365 \times 10^5$ for the red channel centered at 640 nm, $5.9796 \times 10^5$ for the first green channel centered at 540 nm, $5.8939 \times 10^5$ for the second green channel centered at 540 nm, and $5.1837 \times 10^5$ for the blue channel centered at 470 nm, respectively.

Since the PCAMs were not equipped with a calibration target, we used solar irradiance to obtain the reflectance (expressed in terms of the reflectance factor [*Hapke*, 2012]) as

$$r_s = \frac{\pi I_s}{\cos i \int J(\lambda) S(\lambda) \mathrm{d}\lambda}, \tag{2}$$

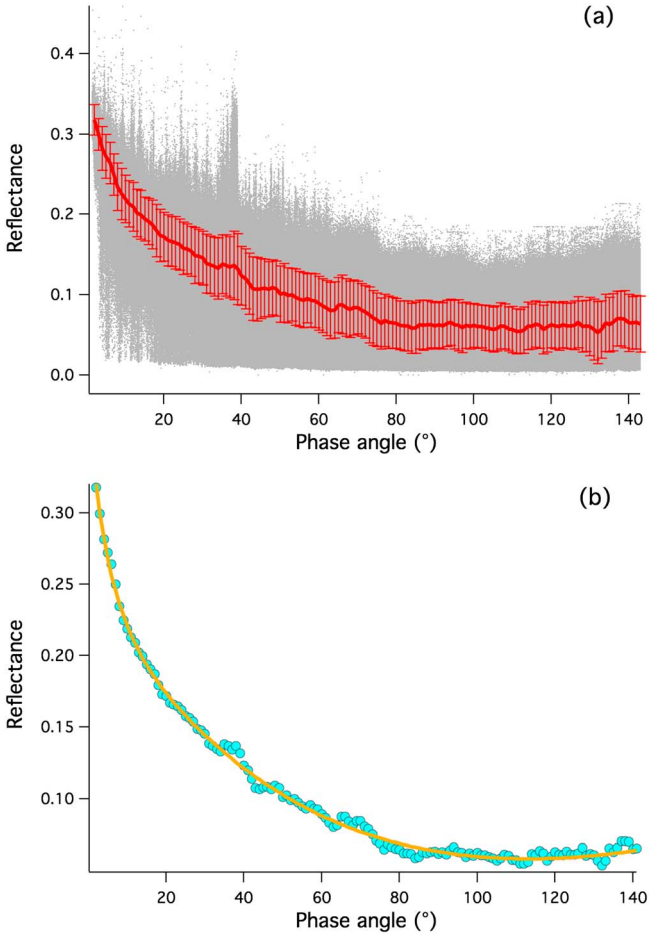


**Figure 3.** In situ phase curve at 640 nm and the Hapke model fitting result. (a) Reflectance at 640 nm corresponding to the areas shown in Figure 2 plotted against phase angle. The dots are the individual reflectance of each pixel and the red line is the average with one standard deviation. Pixels containing resolvable fragments and tiny craters are excluded. (b) In situ phase curve at 640 nm and the results of fitting to the nine-parameter Hapke photometric model.

where $J(\lambda)$ is the solar irradiance reaching the surface [*Gueymard*, 2004], $S(\lambda)$ is the normalized spectral response of the sensor, and $i$ is the solar zenith angle, respectively. The preflight-measured CE3 PCAM sensor spectral response $S(\lambda)$, provided by the payload team, is approximated by Gaussian functions centered at each band's center wavelength.

The retrieved phase curve in reflectance in 640 nm is plotted as grey dots in Figure 3a. Although keeping only the brightest pixels such as those on the top envelop of the phase curve can make the phase curve to have a higher signal-to-noise ratio (SNR) [e.g., *Abe et al.*, 2006] as in the shot-noise limit the SNR is proportional to the square root of the signal strength, keeping all pixels can retain the information of all particles imaged by the PCAM. It also should be noted that although the phase angle range extends to 149° in Figure 2, we only keep the data below 141° as the images with phase angles higher than 141° contain specular reflections of the rover surface (Figure S3 in the supporting information) and have low SNR values. By averaging the reflectance values of pixels within 1° phase angle range, the final phase curve with one standard deviation can be obtained, as shown as the red line in Figure 3a for the 640 nm channel. The color variations of the phase curve will be discussed in section 5.

## 3. Photometric Inversions Using the Hapke Model

Although the accuracy of approximation photometric models especially for high albedo surfaces has been in debate [e.g., *Mishchenko*, 1994; *Hapke*, 1996; *Hapke et al.*, 2009; *Zhang and Voss*, 2011; *Shkuratov et al.*, 2012; *Hapke*, 2013], their closed form permits an easy inversion to infer the physical properties of the regolith. We used the nine-parameter Hapke model [*Hapke*, 2012; *Hapke et al.*, 2012] to fit the extracted phase curve using a nonlinear least squares method. Since the phase-reddening effect is very weak (section 5) and the four spectral bands are overlapping, we concentrate the quantitative analysis on the red phase curve (640 nm) shown in Figure 3. The most recent version of the Hapke model expressed in reflectance factor is

$$r_s(\mu_0,\mu,\alpha) = K\frac{\varpi_0}{4\mu_0}\frac{\mu_{0e}}{\mu_{0e}+\mu_e}\{[1+B_S(\alpha)]P(\alpha)+H(\mu_{0e}/K)H(\mu_e/K)-1\}[1+B_C(\alpha)]S\left(i,e,\psi\overline{\theta}\right), \quad (3)$$

where $K$ is the porosity coefficient, $\varpi_0$ is the particle single-scattering albedo, $\mu_{0e}$ and $\mu_e$ are the effective cosines of the incident and viewing zenith angles, and

$$\mu_0 = \cos i,$$

$$H(x) \approx \frac{1}{1-\varpi_0 x\left(r_0+\frac{1-2r_0x}{2}\ln\frac{1+x}{x}\right)},$$

where $r_0$ is the diffusive reflectance given by

$$r_0 = \frac{1-\sqrt{1-\varpi_0}}{1+\sqrt{1-\varpi_0}}.$$

The functions $B_S(\alpha)$ and $B_C(\alpha)$ describe the SHOE and CBOE at small phase angles, respectively, as

$$B_S(\alpha) = \frac{B_{S0}}{1+\frac{1}{h_S}\tan\left(\frac{\alpha}{2}\right)},$$

$$B_C(\alpha) = B_{C0}\frac{1+|1-\exp(-\zeta)|/\zeta}{2|1+\zeta|^2},$$

$$\zeta = \frac{\tan(\alpha/2)}{h_C},$$

and $S(i,e,\psi\overline{\theta})$ is the surface roughness factor with an average subpixel surface slope angle $\overline{\theta}$ [*Hapke*, 2012]. The single-particle scattering phase function $P(\alpha)$ can be approximated by a two-parameter Henyey-Greenstein phase function as

$$P(\alpha) = \frac{1+c}{2}\frac{1-b^2}{\left(1-2b\cos\alpha+b^2\right)^{3/2}} + \frac{1-c}{2}\frac{1-b^2}{\left(1+2b\cos\alpha+b^2\right)^{3/2}}, \tag{4}$$

where $b$ and $c$ are empirical parameters. At rather small $\varpi_0$ (the lunar case) the normal albedo $A_n$ of a planetary surface may be approximated by the Hapke parameters as

$$A_n \approx \frac{\varpi_0}{8}(1+B_{S0})(1+B_{C0})P(0), \tag{5}$$

where $P(0)$ is single-scattering phase function at zero phase angle. The fitting parameters used in this work are thus $K$, $\varpi_0$, $b$, $c$, $B_{S0}$, $h_S$, $B_{C0}$, $h_C$, and $\overline{\theta}$ and their interpretations are briefly outlined below.

For equant particles much larger than radiation wavelength, $K$ may be expressed in terms of the filling factor $\phi$ as

$$K = -\frac{\ln\left(1-1.209\phi^{2/3}\right)}{1.209\phi^{2/3}}. \tag{6}$$

The single-scattering albedo $\varpi_0$ is the ratio of the particle scattering efficiency and extinction efficiency and can approach 1 for nearly nonabsorbing grains and several percent for charcoal black materials. Parameters $b$ and $c$ control the backscattering or forward scattering nature of a single scatter. The parameter $B_{S0}$ is a measure of the transparency feature of the scatter and is 1 for totally opaque grains and close to 0 for transparent grains. The parameter $h_S$ is closely related to the regolith filling factor $\phi$ and size distribution $N(d)$. For the typical lunar regolith with a power law size distribution $N(d) \sim d^{-4}$ [*McKay et al.*, 1974], $h_S$ is given by

$$h_S \approx -0.537\frac{\ln\left(1-1.209\phi^{2/3}\right)}{\ln(d_l/d_s)}\phi^{1/3}, \tag{7}$$

where $d_l$ and $d_s$ are the largest and smallest grain sizes, respectively [*Hapke*, 2012]. The physical meaning of $B_{C0}$ is still in debate and it is probably related to the brightness of the surface. The parameter $h_C$ is related to the photon transport mean free path $\Lambda_T$ through [*Hapke*, 2012]

$$\Lambda_T \sim \frac{\lambda}{4\pi h_C}, \tag{8}$$

where $\lambda$ is the radiation wavelength. Since equation (8) has only been quantitatively verified for colloidal suspensions of well-separated spherical particles but not for media of closely packed irregular particles such as the lunar regolith, $\Lambda_T$ is only used to estimate the order of magnitude of the average distance between particles and hence the average particle size responsible for the coherent backscattering (CBS) effect. The slope angle $\overline{\theta}$ describes the subpixel roughness feature of a terrain. In general, resurfacing processes such as volcanism and dust blowing would smooth a surface while frequent meteorite bombardment would roughen a surface. By using the Apollo Lunar Surface Closeup Camera pictures of the lunar surface, *Helfenstein and Shepard* [1999] have estimated that the average RMS slope angles for lunar highland and mare regolith are $\overline{\theta} = 27 \pm 1°$ and $\overline{\theta} = 24 \pm 1°$, respectively. Although the study area in this work is very flat with maximum

elevation fluctuations less than 1 m as evidenced by the DEM data (Figure 1b), the subpixel roughness term with the average slope angle $\overline{\theta}$ is included as this term may operate down to millimeter or smaller levels.

The nine-parameter model given by equation (3) is highly nonlinear except for $\varpi_0$ and at least some of the parameters are sensitive to the initial guess values in the fitting. To avoid ambiguous and unphysical results as much as possible, we followed the approach used by *Hapke et al.* [2012] and the detailed procedures are given in the supporting information. The final fitting results are as follows: $\varpi_0 = 0.19^{+0.1}_{-0.3}$, $b = 0.30 \pm 0.1$, $c = 0.08^{+0.12}_{-0.08}$, $K = 1.47^{+0.16}_{-0.07}$, $\overline{\theta} = 17^{\circ+1^{\circ}}_{-6^{\circ}}$, $B_{S0} = 0.52^{+0.3}_{-0.2}$, $h_S = 0.059 \pm 0.01$, $B_{C0} = 0.47^{+0.15}_{-0.17}$, $h_C = 0.12 \pm 0.01$, and $A_n = 0.15^{+0}_{-0.05}$. The plain numbers indicate the best fitting values and the upper and lower bounds indicate the possible ranges of values estimated from Figure S5 in the supporting information. The fitting result is displayed in Figure 3b. The obtained normal albedo $A_n$ is close to that observed in lunar maria at 640 nm from the Earth [*Velikodsky et al.*, 2011]. The $h_C$ value implies, through equation (8), that the particles responsible for the CBOE are ~0.4 μm, corresponding to submicroscopic dust grains present in the landing area, though observational data show that CBOE should be small for such dark surfaces [*Shkuratov et al.*, 2012; *Kaydash et al.*, 2013a]. By using equations (6) and (7), the filling factor $\phi$ corresponding to $K = 1.47$ is 0.32, and the ratio of the largest and smallest particle diameters $d_l/d_s$ corresponding to $h_S \sim 0.059$ is ~180. If we assume the smallest grains that can cast shadows are 20 μm, the largest particles responsible for the SHOE effect are ~4 mm. The derived filling factor value, $0.32^{+0.11}_{-0.05}$, is smaller than the best estimate value of the Apollo in situ measurement for depth range 0–15 cm, 0.48 ± 0.02, [*Carrier et al.*, 1991], and is thus plausible as the topmost layers that visible radiation can penetrate should be more porous. Compared with the average mare region (24 ± 1°), the lower $\overline{\theta}$ value (11°–18°) retrieved indicates the smoother nature of the landing site. This result is consistent with the smoother surfaces blown by landing spacecraft as revealed by phase ratio imagery [*Shkuratov et al.*, 2011, 2013].

## 4. Comparisons With Spaceborne Measurements

Compared with our in situ phase curve analysis which used a nine-parameter Hapke model, most workers working on lunar and asteroid photometry have used a more simplified version. For example, *Hapke et al.* [2012] assumed $c = 1$, $K = 1$, and $S = 1$ in equation (3) in analyzing the LRO Wide Angle Camera (WAC) data by arguing that the forward scattering lobe is absent within the 120° phase angle range of the data set they used and for the nadir-viewing WAC sensor the roughness effect can be ignored; *Sato et al.* [2014] mapped the Hapke parameters over the Moon by using a SHOE-only version with further simplifications by correlating $B_{S0}$ with $\varpi_0$ and relating $b$ with $c$ through an empirical relationship ("Hockey stick," equation (9) below) and thus their model is essentially a three-parameter version of equation (3). Most workers analyzing photometric data of dark asteroids (e.g., 1 Ceres) ignore the coherent backscattering enhancement effect in the Hapke model and assume a backscattering phase function, thus leaving only five parameters ($\varpi_0$, $b$, $B_{S0}$, $h_S$, and $\overline{\theta}$) in equation (3) [e.g., *Li et al.*, 2006]. It thus would be instructive to use a SHOE-only version and compare the current in situ results with remote measurements such as that done by *Sato et al.* [2014] using the LRO data. By using the five-parameter version of equation (3) ($\varpi_0$, $b$, $c$, $B_{S0}$, and $h_S$) and fixing $\overline{\theta} = 23.4°$ as *Sato et al.* [2014] did, we obtained: $\varpi_0 = 0.33 \pm 0.00$, $b = 0.32 \pm 0.01$, $c = -0.17 \pm 0.02$, $B_{S0} = 1.28 \pm 0.07$, and $h_S = 0.03 \pm 0.01$. The reason that we did not use the Hockey Stick relation

$$c = 3.29e^{-17.4b^2} - 0.908, \tag{9}$$

to derive $c$ from $b$ is that we would not make a prior assumption that the $b$ and $c$ values retrieved from the current in situ phase curve should fall into the known $b$ and $c$ library values based on which equation (9) was derived. We also did not use the correlation between $\varpi_0$ and $B_{S0}$ derived by *Sato et al.* [2014] as their phase angle range is within 97°, while our data reaches out to 141°. Comparison of our results with Sato et al.'s average maria results (Table S2 in the supporting information) shows that (1) our $\varpi_0$ value, 0.33, is larger than their value 0.24, indicating that we are seeing brighter grains in the landing site; (2) our $b$ and $c$ values are very close to the typical highland crystalline and mare crystalline in the Hockey stick graph; (3) our $h_S$ value 0.03 is smaller than the average maria value of 0.05, indicating we are seeing a broader size distribution in the in situ phase curve; (4) our smaller $B_{S0}$ value 1.28, as compared to the much larger $B_{S0}$ value 2.0 for the average maria region, may indicate we are seeing more transparent grains. The five-parameter Hapke model fitting also implies that the SHOE alone may not completely account for the OE as the $B_{S0}$ value

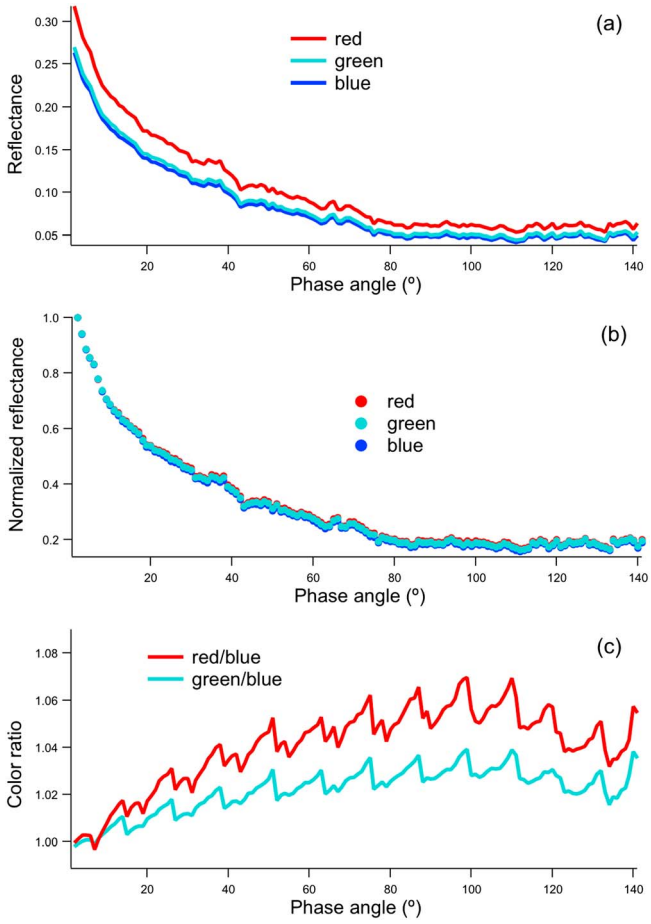


**Figure 4.** Phase curves in different colors and color ratios, red (640 nm), green (the average of two 540 nm channels), and blue (470 nm). (a) Reflectance, (b) reflectance normalized at 2° phase angle, and (c) ratios of red over blue and green over blue. The error bars are not shown here for clarity.

is larger than 1. Thus, the effect of coherent backscattering enhancement should be present in the opposition spike in the CE3 landing site or the model is not entirely adequate [*Shkuratov et al.*, 2012].

## 5. Phase-Reddening Effect

Since many regions of the lunar surface have been found to exhibit a prominent phase-reddening effect when observed from space, i.e., shorter wavelength phase curves are steeper than the longer wavelength ones [e.g., *Kaydash et al.*, 2010, 2013a], it would be interesting to see if the in situ phase curve has this effect or not. The extracted in situ phase curves in three different colors are shown in Figure 4. It is seen that the red reflectance has the highest values while the blue one is the lowest and when normalized to 2° phase angle, the three colors reflectance almost lay on top of each other, though the blue curve is about 6% steeper than the red one at phase angle 100° as shown in Figure 4c. The weakness of the phase-reddening effect observed by the PCAMs can be related to the broad and overlapping spectral responses of the three color bands [*Ren et al.*, 2014] which could have averaged this effect out. The oscillating structures shown in Figure 4c were found to be caused by uncertainties of the inner and exterior orientation elements recorded in the PCAM image header files and the retrieved viewing zenith angles have similar oscillating behavior (Figure S6 and supporting information). The resultant uncertainty in the retrieved emergence angle and phase angle is about 1°. Nevertheless, it appears that the phase-reddening effect is present in the in situ phase curve. Earlier, this was found in photometric laboratory measurements of lunar samples [*Shkuratov et al.*, 1996]. We did not detect the color opposition effect that points out to the existence of coherent backscattering enhancement [*Shkuratov et al.*, 2011; *Kaydash et al.*, 2013a].

## 6. Summary and Conclusions

We have extracted the first in situ lunar phase curve since the Apollo era and performed the photometric inversions to infer the regolith physical properties. To the best of our knowledge, the current in situ phase curve has covered larger phase angle range, up to 141°, as compared with previous Apollo in situ [*Pohn et al.*, 1969; *Rennilson et al.*, 1968] and modern spaceborne measurements [e.g., *Hapke et al.*, 2012; *Sato et al.*, 2014]. This has enabled us to perform reliable photometric inversions, and we have found that the lunar regolith does have a forward lobe in the single-scattering phase function and the coherent backscattering may exist in the relatively brighter mare regions. Comparisons of the ground-truth measurement with spaceborne phase curve measurements show that the grains in the landing site are brighter, more transparent, and appear to be better crystallized than the average maria basaltic grains. These results are also consistent with the spectroscopic results that show the in situ data have stronger mineral absorption features than the remote measurements [*Zhang et al.*, 2015]. We demonstrated that in situ measurements are very important

as they can reveal surface features that are not detected by orbital measurements. The current phase curve can be used as the ground-truth validations of any future spaceborne phase curve measurement over the landing site region.

**Acknowledgments**
H.Z. thanks Harrison Schmitt for helpful discussions. We thank Bruce Hapke and an anonymous reviewer for critical and constructive comments which improved the quality of this paper. All the Chang'E-3 data used in this work can be obtained from http://www.bao.ac.cn/. This work was supported by the National Natural Science Foundation of China (41071229 and 41276180) and by the Key Research Program of the Chinese Academy of Sciences (KGZD-EW-603).

The Editor thanks Augustin Jehl and an anonymous reviewer for their assistance in evaluating this paper.

## References

Abe, M., Y. Takagi, K. Kitazato, S. Abe, T. Hiroi, F. Vilas, B. Clark, P. Abell, S. Lederer, and K. Jarvis (2006), Near-infrared spectral results of asteroid Itokawa from the Hayabusa spacecraft, *Science*, *312*, 1334–1338.

Buratti, B. J., J. K. Hillier, and M. Wang (1996), The lunar opposition surge: Observations by Clementine, *Icarus*, *124*, 490–499, doi:10.1006/icar.1996.0225.

Carrier, W. D., III, G. R. Olhoeft, and W. Mendell (1991), Physical properties of the lunar surface, in *Lunar Sourcebook*, edited by G. H. Heiken, D. T. Vaniman, and B. M. French, pp. 475–594, Cambridge Univ. Press, Cambridge, U. K.

Dollfus, A., and E. Bowell (1971), Polarimetric properties of the lunar surface and interpretation. I. Telescope observation, *Astron. Astrophys.*, *10*, 29–53.

Gueymard, C. A. (2004), The sun's total and spectral irradiance for solar energy applications and solar radiation models, *Sol. Energy*, *76*, 423–453.

Hapke, B. (1996), Are planetary regolith particles backscattering? Response by a paper by M. Mishchenko, *J. Quant. Spectros. Radiat. Transfer*, *55*, 837–848.

Hapke, B. (2012), *Theory of Reflectance and Emittance Spectroscopy*, Cambridge Univ. Press, Cambridge, U. K.

Hapke, B. (2013), Comment on "A critical assessment of the Hapke photometric model" by Y. Shkuratov et al, *J. Quant. Spectros. Radiat. Transfer*, *116*, 184–190, doi:10.1016/j.jqsrt.2012.11.002.

Hapke, B., M. Shepard, R. Nelson, W. Smythe, and J. Piatek (2009), A quantitative test of the ability of models based on the equation of radiative transfer to predict the bidirectional reflectance of a well-characterized medium, *Icarus*, *199*, 210–218.

Hapke, B., B. Denevi, H. Sato, S. Braden, and M. Robinson (2012), The wavelength dependence of the lunar phase curve as seen by the Lunar Reconnaissance Orbiter wide angle camera, *J. Geophys. Res.*, *117*, E00H15, doi:10.1029/2011JE003916.

Helfenstein, P., and M. K. Shepard (1999), Submillimeter-scale topography of the lunar regolith, *Icarus*, *141*, 107–131.

Kaydash, V. G., S. Y. Gerasimenko, Y. G. Shkuratov, N. V. Opanasenko, Y. I. Velikodsky, V. V. Korokhin, and M. V. Kaydash (2010), The phase ratios of the color index: Mapping of two regions of the near side of the Moon, *Sol. Syst. Res.*, *44*, 267–280, doi:10.1134/S0038094610040015.

Kaydash, V., C. Pieters, Y. Shkuratov, and V. Korokhin (2013a), Lunar opposition effect as inferred from Chandrayaan-1 M3 data, *J. Geophys. Res. Planets*, *118*, 1221–1232, doi:10.1002/jgre.20098.

Kaydash, V., Y. Shkuratov, and G. Videen (2013b), Landing of the probes Luna 23 and Luna 24 remains an enigma, *Planet. Space Sci.*, *89*, 172–182.

Li, J.-Y., L. A. McFadden, J. W. Parker, E. F. Young, S. A. Stern, P. C. Thomas, C. T. Russell, and M. V. Sykes (2006), Photometric analysis of 1 Ceres and surface mapping from HST observations, *Icarus*, *182*, 143–160.

McKay, D. S., R. M. Fruland, and G. H. Heiken (1974), Grain size and the evolution of lunar soils, in *Proceedings of the Fifth Lunar Science Conference*, edited by W. Gose, pp. 887–906, Pergamon, New York.

Mishchenko, M. I. (1994), Asymmetry parameters of the phase function for densely packed scattering grains, *J. Quant. Spectros. Radiat. Transfer*, *52*, 95–110, doi:10.1016/0022-4073(94)90142-2.

Ohtake, M., C. Pieters, P. Isaacson, S. Besse, Y. Yokota, T. Matsunaga, J. Boardman, S. Yamomoto, J. Haruyama, and M. Staid (2013), One Moon, many measurements 3: Spectral reflectance, *Icarus*, *226*, 364–374, doi:10.1016/j.icarus.2013.05.010.

Pohn, H. A., H. W. Radin, and R. L. Wildey (1969), The Moon's photometric function l, near zero phase angle from Apollo 8 photography, *Astrophys. J.*, *157*, L193–L195.

Ren, X., C.-L. Li, J.-J. Liu, F.-F. Wang, J.-F. Yang, E.-H. Liu, B. Xue, and R.-J. Zhao (2014), A method and results of color calibration for the Chang'E-3 terrain camera and panoramic camera, *Res. Astron. Astrophys.*, *14*, 1557–1566.

Rennilson, J. J., H. E. Holt, and E. C. Morris (1968), In situ measurements of the photometric properties of an area on the lunar surface, *J. Opt. Soc. Am.*, *58*, 747–755.

Sato, H., M. Robinson, B. Hapke, B. Denevi, and A. Boyd (2014), Resolved Hapke parameter maps of the Moon, *J. Geophys. Res. Planets*, *119*, 1775–1805, doi:10.1002/2013JE004580.

Shkuratov, Y. G., L. Y. Melkumova, N. V. Opanasenko, and D. G. Stankevich (1996), Phase dependence of the color index of solid surfaces of celestial bodies, *Sol. Syst. Res.*, *30*, 71–79.

Shkuratov, Y., V. Kaydash, V. Korokhin, Y. Velikodsky, N. Opanasenko, and G. Videen (2011), Optical measurements of the Moon as a tool to study its surface, *Planet. Space Sci.*, *59*, 1326–1371.

Shkuratov, Y., V. Kaydash, D. Petrov, V. Korokhin, D. Stankevich, and G. Videen (2012), A critical assessment of the Hapke photometric model (2012), *J. Quant. Spectrosc. Radiat. Transfer*, *113*, 2431–2456.

Shkuratov, Y., V. Kaydash, X. Sysolyatina, A. Razim, and G. Videen (2013), Lunar surface traces of engine jets of Soviet sample return probes: The enigma of Luna-23 and Luna-24 landing sites, *Planet. Space Sci.*, *75*, 28–36.

Shkuratov, Y., N. Opanasenko, V. Korokhin, and G. Videen (2015), The Moon, in *Polarimetry of Stars and Planetary Systems*, edited by L. Kolokolova, J. Hough, and A.-C. Levasseur-Regound, Cambridge Univ. Press, Cambridge, U. K.

Tan, X., J.-J. Liu, C.-L. Li, J.-Q. Feng, X. Ren, F.-F. Wang, W. Yan, W. Zuo, X.-Q. Wang, and Z.-B. Zhang (2014), Scientific data products and the data pre-processing subsystem of the Chang'e-3 mission, *Res. Astron. Astrophys.*, *14*, 1682–1694, doi:10.1088/1674-4527/14/12/016.

Velikodsky, Y. I., N. V. Opanasenko, L. A. Akimov, V. V. Korokhin, Y. G. Shkuratov, V. G. Kaydash, G. Videen, S. A. Ehgamberdiev, and N. E. Berdalieva (2011), New Earth-based absolute photometry of the Moon, *Icarus*, *214*, 30–45.

Xiao, L., P. Zhu, G. Fang, Z. Xiao, Y. Zou, J. Zhao, N. Zhao, Y. Yuan, L. Qiao, and X. Zhang (2015), A young multilayered terrane of the northern Mare Imbrium revealed by Chang'E-3 mission, *Science*, *347*, 1226–1229.

Yokota, Y., et al. (2011), Lunar photometric properties at wavelengths 0.5–1.6 μm acquired by SELENE Spectral Profiler and their dependency on local albedo and latitudinal zones, *Icarus*, *215*, 639–660.

Zhang, H., and K. J. Voss (2011), On Hapke photometric model predictions on reflectance of closely packed particulate layers, *Icarus*, *215*, 27–33, doi:10.1016/j.icarus.2011.07.022.

Zhang, H., et al. (2015), In situ optical measurements of Chang'E-3 landing site in Mare Imbrium: 1. Mineral abundances inferred from spectral reflectance, *Geophys. Res. Lett.*, *42*, 6945–6950, doi:10.1002/2015GL065273.